The Astrophysical Journal, 640:539–552, 2006 April 1

PROBING GALAXY FORMATION WITH He II COOLING LINES

Yujin Yang, Ann I. Zabludoff, Romeel Davé, Daniel J. Eisenstein, and Philip A. Pinto
Steward Observatory, University of Arizona, Tucson, AZ 85721; yyang@as.arizona.edu, azabludoff@as.arizona.edu, rad@as.arizona.edu, deisenstein@as.arizona.edu, ppinto@as.arizona.edu

Neal Katz
Astronomy Department, University of Massachusetts, Amherst, MA 01003; nsk@kaka.astro.umass.edu

David H. Weinberg
Department of Astronomy, Ohio State University, Columbus, OH 43210; dhw@astronomy.ohio-state.edu

and

Elizabeth J. Barton
Department of Physics and Astronomy, University of California, Irvine, CA 92697; ebarton@uci.edu
Received 2005 July 15; accepted 2005 August 31

ABSTRACT

Using high-resolution cosmological simulations, we study hydrogen and helium gravitational cooling radiation from gas accretion by young galaxies. We focus on the He II cooling lines, which arise from gas with a different temperature history ($T_{\max} \sim 10^5$ K) than H I line–emitting gas. We examine whether three major atomic cooling lines, H I λ1216, He II λ1640, and He II λ304, are observable, finding that Lyα and He II λ1640 cooling emission at $z = 2$–3 are potentially detectable with deep narrowband ($R > 100$) imaging and/or spectroscopy from the ground. While the expected strength of H I λ1216 cooling emission depends strongly on the treatment of the self-shielded phase of the IGM in the simulations, our predictions for the He II λ1640 line are more robust, because the He II emissivity is negligible below $T \sim 10^{4.5}$ K and less sensitive to the UV background. Although He II λ1640 cooling emission is fainter than Lyα by at least a factor of 10 and, unlike Lyα, might not be resolved spatially with current observational facilities, it is more suitable to study gas accretion in the galaxy formation process because it is optically thin and less contaminated by the recombination lines from star-forming galaxies. The He II λ1640 line can be used to distinguish among mechanisms for powering the so-called Lyα blobs—including gravitational cooling radiation, photoionization by stellar populations, and starburst-driven superwinds—because (1) He II λ1640 emission is limited to very low metallicity [$\log (Z/Z_\odot) \lesssim -5.3$] and Population III stars and (2) the blob's kinematics are probed unambiguously through the He II line width, which for cooling radiation is narrower ($\sigma < 400$ km s^{-1}) than typical wind speeds.

Subject headings: cosmology: theory — galaxies: formation — intergalactic medium

Online material: color figures

1. INTRODUCTION

Galaxies grow partly by accretion of gas from the surrounding intergalactic medium and partly by mergers with other galaxies. Observational studies of galaxy assembly have focused primarily on merger rates, which can be measured indirectly by counting close pairs and merger remnants. However, all the mass that enters the galaxy population ultimately does so by accretion, and mergers can only redistribute this mass from smaller systems to larger systems. Furthermore, numerical simulations predict that even large galaxies grow primarily by smooth gas accretion rather than by cannibalism of smaller objects (Murali et al. 2002; Keres et al. 2005). Gas shock-heated to the virial temperature of a typical dark matter halo would radiate most of its acquired gravitational energy in the soft X-ray continuum, making individual sources very difficult to detect, especially at high redshift. However, Fardal et al. (2001, hereafter F01) show that much of the gas that enters galaxies in hydrodynamic cosmological simulations never heats to high temperatures at all and that it therefore channels a substantial fraction of its cooling radiation into atomic emission lines, especially H I Lyα. F01 and Haiman et al. (2000) suggested that extended "Lyα blobs" (e.g., Keel et al. 1999; Steidel et al. 2000; Francis et al. 2001; Matsuda et al. 2004; Dey et al. 2005), with typical sizes of 10″–20″ and line luminosities $L_{\mathrm{Ly}\alpha} \sim 10^{44}$ ergs s^{-1}, might be signatures of cooling radiation from forming galaxies. Furlanetto et al. (2005) have also investigated predictions for Lyα cooling radiation from forming galaxies in hydrodynamic simulations.

In this paper, we investigate other aspects of cooling radiation from forming galaxies, in particular the potentially detectable radiation in the He II λ304 (Lyα) and He II λ1640 (Hα) lines of singly ionized helium. While challenging, the successful detection He II line emission would complement H I Lyα measurements in at least three ways. First, because H I and He II line cooling rates peak at different temperatures ($T \sim 10^{4.3}$ vs. $\sim 10^5$ K), measurements of both lines could constrain the physical conditions of the emitting gas. Recent theoretical studies imply that "cold mode" accretion, in which the maximum gas temperature is well below the halo virial temperature, is a ubiquitous and fundamental feature of galaxy formation (F01; Katz et al. 2003; Birnboim & Dekel 2003; Keres et al. 2005; Dekel & Birnboim 2004), a view anticipated by the early analytical work of Binney (1977). Simultaneous measurements of He II and H I emission from different types of galaxies could eventually test detailed predictions for the temperature distribution of cooling gas.

The second advantage of the He II λ1640 line is that it should be optically thin, allowing a straightforward interpretation of the observed emission in terms of the spatial distribution and kinematics of the cooling gas. In contrast, the radiative transfer effects on the H I Lyα emission from accreting gas are more complicated, an issue that we will investigate in future work (J. Kollmeier et al. 2006, in preparation; see also Cantalupo et al. 2005).

Third, the different temperature dependence and absence of radiative transfer effects in He II lines could help distinguish cooling radiation from alternative explanations of Lyα blobs, such as emission from collisionally ionized gas in galactic superwinds (Taniguchi & Shioya 2000) or from gas photoionized by young stellar populations. For example, only the lowest metallicity stars ($\log Z/Z_\odot \lesssim -5.3$) have hard enough spectra to ionize He II to He III, so stellar photoionization will generally not produce He II line emission.

It is possible that He II cooling emission from forming galaxies at high redshift has already been detected. One such example is the broad He II λ1640 line in the composite spectrum of Lyman break galaxies (LBGs) from Shapley et al. (2003). The composite He II line shows a rather broad line width (FWHM $\sim$ 1500 km s^{-1}), which is a possible signature of Wolf-Rayet (W-R) stars. However, it is difficult to reproduce the strength of the He II line via stellar population models with reasonable parameters (Shapley et al. 2003). We show in this paper that the He II cooling emission around individual galaxies is detectable, which suggests it might be fruitful to search for He II λ1640 cooling emission in the outer parts of individual LBGs.

The next section describes our simulations and the radiative cooling mechanisms that lead to H I λ1216, He II λ1640, and He II λ304 line emission. We present H I λ1216 and He II λ1640 cooling maps in § 3.1 and discuss the properties of the cooling radiation sources in § 3.2. In § 3.3, we examine the detectability of the three major cooling lines in the far-ultraviolet and optical and discuss the best observational strategies. In § 4, we discuss mechanisms other than gravitational cooling radiation that can generate extended Lyα emission, and we describe how the He II cooling line might help us discriminate among those mechanisms. We summarize our conclusions in § 5.

2. SIMULATIONS AND COOLING RADIATION

We use PTreeSPH (parallel tree smoothed particle hydrodynamics) simulations (Davé et al. 1997) including the effects of radiative cooling, star formation, thermal feedback, and a spatially uniform metagalactic photoionizing background. We analyze two simulations: one with a cubic volume of 11.111 h^{-1} Mpc (comoving) on a side and a spatial resolution of 1.75 h^{-1} kpc (comoving; equivalent Plummer softening), the other with a cubic volume of 22.222 h^{-1} Mpc on a side and 3.5 h^{-1} kpc resolution. Hereafter, we refer to these two simulations as the 11 Mpc and 22 Mpc simulations, respectively. The simulations consist of 128^3 dark matter particles and 128^3 gas particles, giving a mass resolution of $m_{\rm SPH} = 1.3 \times 10^7\ M_\odot$ and $m_{\rm dark} = 10^8\ M_\odot$ for the 11 Mpc simulation and $m_{\rm SPH} = 1.1 \times 10^8\ M_\odot$ and $m_{\rm dark} = 7.9 \times 10^8\ M_\odot$ for the 22 Mpc simulation. We adopt a ΛCDM cosmology with the parameters $\Omega_{M=0.4}$, $\Omega_\Lambda = 0.6$, $\Omega_b h^2 = 0.02$, and $H_0 = 65$ km s^{-1} Mpc^{-1}. In our calculation of cooling emission lines, we basically follow the radiative cooling processes described in Katz et al. (1996, hereafter KWH96). Here, we briefly summarize the cooling processes that can contribute to line emission.

The four underlying assumptions of radiative cooling are primordial composition, ionization equilibrium, an optically thin gas, and a spatially uniform radiation field. In the simulations, we adopt $X = 0.76$ and $Y = 0.24$, where X and Y are the hydrogen and helium abundance by mass. The abundances of each ionic species (H^0, H^+, He^0, He^+, He^{++}) are solely determined by assuming that the primordial plasma is optically thin and in ionization equilibrium (but not in thermal equilibrium).

The functional forms of the temperature-dependent recombination rates, collisional ionization rates, collisional excitation rates, and the rate equations are given in § 3 of KWH96 and the tables therein. The uniform photoionizing UV background is taken from Haardt & Madau (1996).

In the next section, we describe the Lyα and He II cooling curves under the optically thin gas assumption, the assumption used in our simulations. However, in the high-density regime, a gas cloud becomes dense enough to shield the central part of itself from the UV background, i.e., becomes self-shielded. Therefore, the actual emissivity of this self-shielded (or condensed phase) gas is highly uncertain. We discuss below how to treat this phase of the intergalactic medium (IGM) to derive better estimates of the cooling radiation. Once we generate the Lyα and He II cooling emissivities, the cooling radiation is determined by how many gas particles populate a certain range of temperature and density, where we appeal to the high-resolution cosmological simulations mentioned above.

2.1. *Cooling Curves*

Among the various radiative cooling processes, only two can produce H I Lyα (λ1216), He II Lyα (λ304), and He II Baα (λ1640) photons: the recombination cascades of a free electron and the collisional excitation of a bound electron to an excited state followed by radiative decay. The dominant cooling mechanism is the collisional excitation of neutral hydrogen and singly ionized helium, which have their peaks at temperatures of $T \sim 10^{4.3}$ and $\sim 10^5$ K, respectively. Figure 1 shows the H I λ1216 and He II λ304 emissivities for gas of different densities in ionization equilibrium in the presence of a metagalactic photoionizing background. The dashed lines represent the collisional excitation cooling lines of neutral hydrogen and singly ionized helium. The dot-dashed lines and dotted lines denote the recombination lines for these two species due to photoionization and collisional ionization, respectively. The solid lines represent the total Lyα cooling rates of hydrogen and helium. Below $T \sim 10^4$ K, collisions with free electrons are not energetic enough to raise bound electrons to upper levels or to ionize the neutral hydrogen, so the collisional cooling rate of hydrogen drops quickly below this temperature. For singly ionized helium, the collisional cooling rate drops to virtually zero below $T \sim 10^{4.6}$ K. Therefore, below $T \sim 10^4$ K, photoionization by the background UV spectrum (heating) and the following recombination (cooling) is the dominant source for cooling line emission of the primordial plasma.

In the presence of photoionization, the cooling curve depends on the density as shown in Figure 1, because the equilibrium abundances of each species depend on the density. While the collisional ionization rate per unit volume scales as $n_{\rm H}^2$, the photoionization rate per volume is proportional to only $n_{\rm H}$. In low-density gas ($\rho/\bar{\rho}_b \lesssim 10^2$), a significant fraction of H I and He II is photoionized and their abundances are mainly determined by the photoionization process, so the collisional excitation feature is relatively weak. As the gas density increases ($\rho/\bar{\rho}_b \approx 10^3$–$10^4$), however, collisional excitation becomes more important and the cooling curves approach pure collisional equilibrium, the so-called coronal equilibrium. The notable

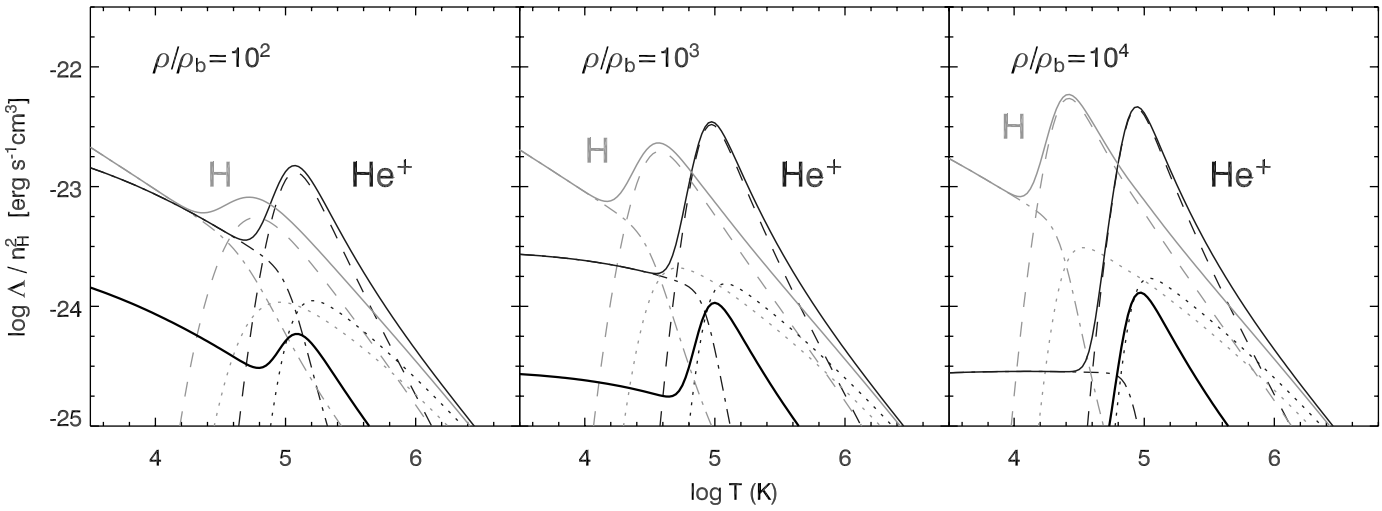

FIG. 1.—Normalized line emissivity $\log \Lambda/n_{\rm H}^2$ as a function of temperature for a primordial plasma at densities $\rho/\bar{\rho}_b = 10^2$, 10^3, and 10^4 (*left to right*) in the presence of a UV ionizing background at $z = 3$. In each panel, the dashed lines represent the collisional excitation cooling rates. The dot-dashed lines and dotted lines denote the recombination rates owing to photoionization and the collisional ionization, respectively. The solid lines represent the total line cooling rates of hydrogen and helium. The bold solid lines below the He II cooling curves represent the He II λ1640 line emissivity. Compared with H I, the cooling rates of He II owing to the UV ionizing background become significantly weaker as the gas density increases. [*See the electronic edition of the Journal for a color version of this figure.*]

difference between the cooling curves of hydrogen and singly ionized helium is that the cooling rates of He II owing to photoionization become significantly weaker as the gas density increases. If we assume that the medium is optically thin to the ionizing background (i.e., not self-shielded) hydrogen is almost fully ionized over the entire temperature range even at high densities, but ~90% of the helium is in a singly ionized state below $T \sim 10^{4.8}$ K at high densities. Thus, the assumption that the gas is optically thin everywhere is roughly valid for the calculation of the He II line fluxes, while it is poor for hydrogen. The correction for the self-shielding of hydrogen is discussed in the next section.

We estimate the He II λ1640 flux from the He II λ304 flux by considering the ratio of He II λ1640 to He II λ304 in the recombination cascades and in the collisional excitations, respectively. The thick solid lines below the He II cooling curves in Figure 1 represent our estimate of the He II λ1640 line emissivity. Below $T \sim 10^5$ K, the optical depth of He II λ304 is so large that case B recombination is a good approximation. Even though the Lyα optical depth is extremely large, the population of the $2p$ and $2s$ states is always much smaller than that of the $1s$ state, because the deexcitation time for level transitions is very short ($A_{2p1s} \approx 10^{10}$ s^{-1}). One might be concerned whether the population of the $2s$ state is large because of the forbidden transition ($2s \rightarrow 1s$), but the two-photon decay process is fast enough to depopulate $2s$ electrons ($A_{2s1s} \simeq 8.22Z^6$ s^{-1}). Therefore, Balmer lines are always optically thin. We adopt $F_{1640}^{\rm rec}/F_{304}^{\rm rec} \simeq 10\%$ by extrapolating the case B values of Storey & Hummer (1995) to the low-density limit. For collisional excitation, we estimate the He II λ1640 flux using

$$\frac{F_{1640}^{\rm coll}}{F_{304}^{\rm coll}} \simeq \frac{C_{1s3s} + C_{1s3p} + C_{1s3d}}{C_{1s2p} + C_{1s3s} + C_{1s3d}} \frac{h\nu_{1640}}{h\nu_{304}}, \quad (1)$$

where C_{ij} is the collisional excitation rate from the i to the j state. We adopt the C_{ij}-values from Aggarwal et al. (1992). $F_{1640}^{\rm coll}/F_{304}^{\rm coll}$ is roughly 2%–4% in the temperature range of $10^5 < T < 10^{5.7}$, where He II λ304 collisional excitation cooling is dominant.

In summary, the He II λ1640 flux is calculated by

$$\varepsilon_{\rm He\,II\,\lambda1640} = f_{\rm rec} n_e n_{\rm He^{++}} \alpha_{\rm He^+}^{\rm rec} h\nu_{\rm Ly\alpha} + f_{\rm coll} n_e n_{\rm He^+} C_{12} h\nu_{\rm Ly\alpha}, \quad (2)$$

where $\alpha_{\rm He^+}^{\rm rec}$ is the recombination rate into $n \geqslant 2$ states of He II and by assuming $f_{\rm rec} \approx 10\%$ and $f_{\rm coll} \approx 2\%$–4%.

2.2. *Self-shielding Correction*

A major difference between our work and that of Fardal et al. (2001) is that our simulations include a uniform UV background radiation field (see also Furlanetto et al. 2005). However, because even state-of-art cosmological simulations like ours do not include radiative transfer, the self-shielded phase of the gas at high column densities is not treated properly. When the gas is heated to a high temperature ($T \sim 10^5$–10^6 K) by falling into the forming galaxy's halo, the gas is mostly ionized, so it is reasonable to assume that the gas is optically thin to the uniform UV background. Subsequently, when the gas cloud starts losing its thermal energy via cooling radiation, its neutral column density becomes sufficiently high that the metagalactic UV radiation cannot penetrate the surrounding gas, and the cloud becomes self-shielded.

Once the supply of ionizing photons is shut off, what happens to the self-shielded high column density clouds? First, the ionization states will achieve collisional ionization equilibrium, where the emissivity is determined solely by collisional ionization and collisional excitation. Second, because the cooling emissivity is boosted by these processes, the self-shielded cloud will cool more rapidly to $T \sim 10^4$ K than it would in the presence of heating by ionizing photons. Below this temperature, the subsequent cooling is dominated by metal lines (if there are metals). Stars ultimately form from this cold gas.

Because our simulations do not include the time evolution of the self-shielded gas or metal-line cooling, it is not clear how long the gas particles stay in the self-shielded phase and emit in collisional ionization equilibrium. The Lyα emissivities shown in Figure 1 become unreliable in this self-shielded regime. Thus, we apply a *pseudo* self-shielding correction to the high-density gas particles to correct their emissivities. This correction is not

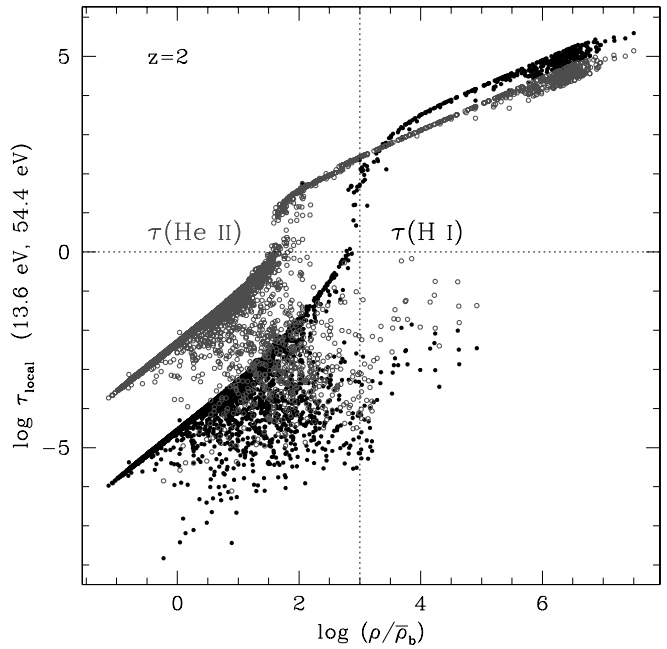

FIG. 2.—Local optical depth of each gas particle as a function of overdensity at $z = 2$. The filled and open circles indicate the optical depth at the H I (13.6 eV) and He II (54.4 eV) ionization edges, respectively. The horizontal and vertical lines represent $\tau = 1$ and $\rho/\bar{\rho}_b \simeq 10^3$, respectively. Note that the H I optical depth increases abruptly at $\rho/\bar{\rho}_b \simeq 10^3$ and the gas becomes self-shielded. [*See the electronic edition of the Journal for a color version of this figure.*]

rigorous; to properly calculate the emissivity of the self-shielded phase of the IGM, one should incorporate a radiative transfer calculation that includes nonuniform and anisotropic UV radiation fields. A different prescription for the self-shielded phase is definitely possible. For example, Furlanetto et al. (2005) consider two extreme cases: (1) adopting zero emissivity and (2) using the collisional ionization equilibrium emissivity for the self-shielded phase. Our self-shielding correction scenario described below lies between these two extremes.

To apply the self-shielding correction, we first define the "local" optical depth for each gas particle, $\tau_{\rm local}(\nu) = \sum_i n_i \sigma_i(\nu)(\alpha l)$, where n_i and σ_i are the number densities and the photoionization cross sections of each species (H^0, He^0, and He^+), respectively. The local size of the gas cloud l (the length that corresponds to the volume that the gas particle would occupy in space) is defined as $(m_{\rm gas}/\rho)^{1/3}$.[1] For each gas particle, the UV background spectrum $J(\nu)$ is attenuated using this local optical depth, i.e., $J(\nu)e^{-\tau(\nu)}$, and new photoionization/heating rates and equilibrium number densities are calculated. We then determine a new $\tau_{\rm local}(\nu)$ from these values and iterate this procedure until the photoionization rates and the optical depths converge. We use these final ionization/heating rates to calculate the Lyα and He II emissivity of each gas particle. This modified emissivity for each gas particle is what we refer to as the *self-shielding correction case*.

In Figure 2, we show the local optical depths of each gas particle in the final equilibrium state as a function of overdensity. For the 22 Mpc simulation at $z = 2$, we show τ(H I) and τ(He II), the optical depth at the H I (13.6 eV) and He II (54.4 eV) ionization edges, respectively. As indicated by the dotted lines, the H I optical depth increases abruptly from $\tau \simeq 1$ to $\tau = 10$–100 at $\rho/\bar{\rho}_b = 10^3$. Therefore, the optically thin UV background assumption is valid below $\rho/\bar{\rho}_b = 10^3$, but the gas becomes self-shielded quickly above this overdensity.

Because the transition from the optically thin case to the self-shielded phase occurs abruptly, we also consider the emissivity of a *condensed phase cut* case as the most conservative for the cooling radiation. There we set the emissivity of the self-shielded gas particles to zero.

Hence, in the following analyses, we consider three possibilities. First is the *optically thin case*, which assumes a spatially uniform UV background for every gas particle. Second is the *self-shielding corrected case* described above, which uses an attenuated UV background for each gas particle appropriate for the local optical depth. Third is the *condensed phase cut case*, in which we set the emissivity of gas with $\log T < 4.5$ and $\rho/\bar{\rho}_b > 10^3$ to zero. We emphasize again that while none of these possibilities is rigorously correct, they range from the most optimistic (1) to the most conservative case (3). Note again that case (1) is appropriate for He II, but the full range of cases should be considered for H I.

3. RESULTS

3.1. *Cooling Maps*

We generate H I λ1216 and He II λ1640 cooling maps at $z = 2$ and 3 by applying our line emissivities to each pixel element and integrating them along the line of sight. The temperature and density of each volume element is computed using the usual SPH smoothing kernels, and the abundances of ionic species are calculated from these smoothed quantities. The thickness of the 11 Mpc simulation along the line of sight is $\Delta z \simeq 0.013$ and 0.019 for $z = 2$ and 3, respectively.

We convert these cooling maps into surface brightness maps using our adopted cosmology. Figure 3 shows the H I λ1216 and He II λ1640 cooling maps for the 11 Mpc simulation at $z = 3$. We show the cooling maps for the condensed phase cut case to represent the most conservative prediction. The left panels show a part $\left(\frac{1}{4} \times \frac{1}{4}\right)$ of our simulation where the filamentary structure of the IGM—the so-called cosmic web—is evident. In the center panels, we show the brightest region (also the most overdense region for $z = 3$) at a finer pixel scale ($\sim 1.5\,h^{-1}$ kpc pixel^{-1}; half of the spatial resolution of our simulation). The right panels show the cooling maps convolved with a 0.″5 FWHM Gaussian filter to mimic a typical ground-based observation.

As shown in Figure 3, the Lyα cooling emission from the IGM is somewhat extended above a surface brightness threshold of 10^{-18} ergs s^{-1} cm^{-2} arcsec^{-2} (the current limit of ground-based detections), whereas the He II emission will be seen almost as a point source. We refer to these extended Lyα cooling sources in our simulations as Lyα blobs. In the cooling maps, we include only Lyα emission from the IGM, not from star formation (i.e., from photoionization caused by massive stars followed by recombination). However, we find a compact group of stars and/or star-forming particles, i.e., galaxies, at the center of each Lyα blob. Therefore, what we would actually observe are galaxies (or Lyα emitters if dust absorption is negligible) embedded within the Lyα blobs.

The most uncertain factor in generating the cooling maps is how much the self-shielded gas contributes to the emission. To quantify this factor globally in the simulations, in Figure 4 we consider the H I λ1216 and He II λ1640 luminosity-weighted

[1] Clumping inside a gas particle and/or among gas particles could be approximated using a free parameter α such that αl represents the effective geometrical edge-to-center distance of the gas cloud. For example, $\alpha_{\rm sphere} = (3/4\pi)^{1/3}$ is given for a single spherical gas cloud, whereas $\alpha = 2$ corresponds to the clumping of $(\alpha/\alpha_{\rm sphere})^3 \simeq 34$ gas particles. The value of α should vary from one particle to another, but we adopt $\alpha = 1$ throughout the paper as a fiducial value. The overdensity where the self-shielding occurs also depends on the choice of the edge-to-center distance αl (and on the redshift). However, we find that the effects of adopting $\alpha = 0.5$–2.0 are insignificant.

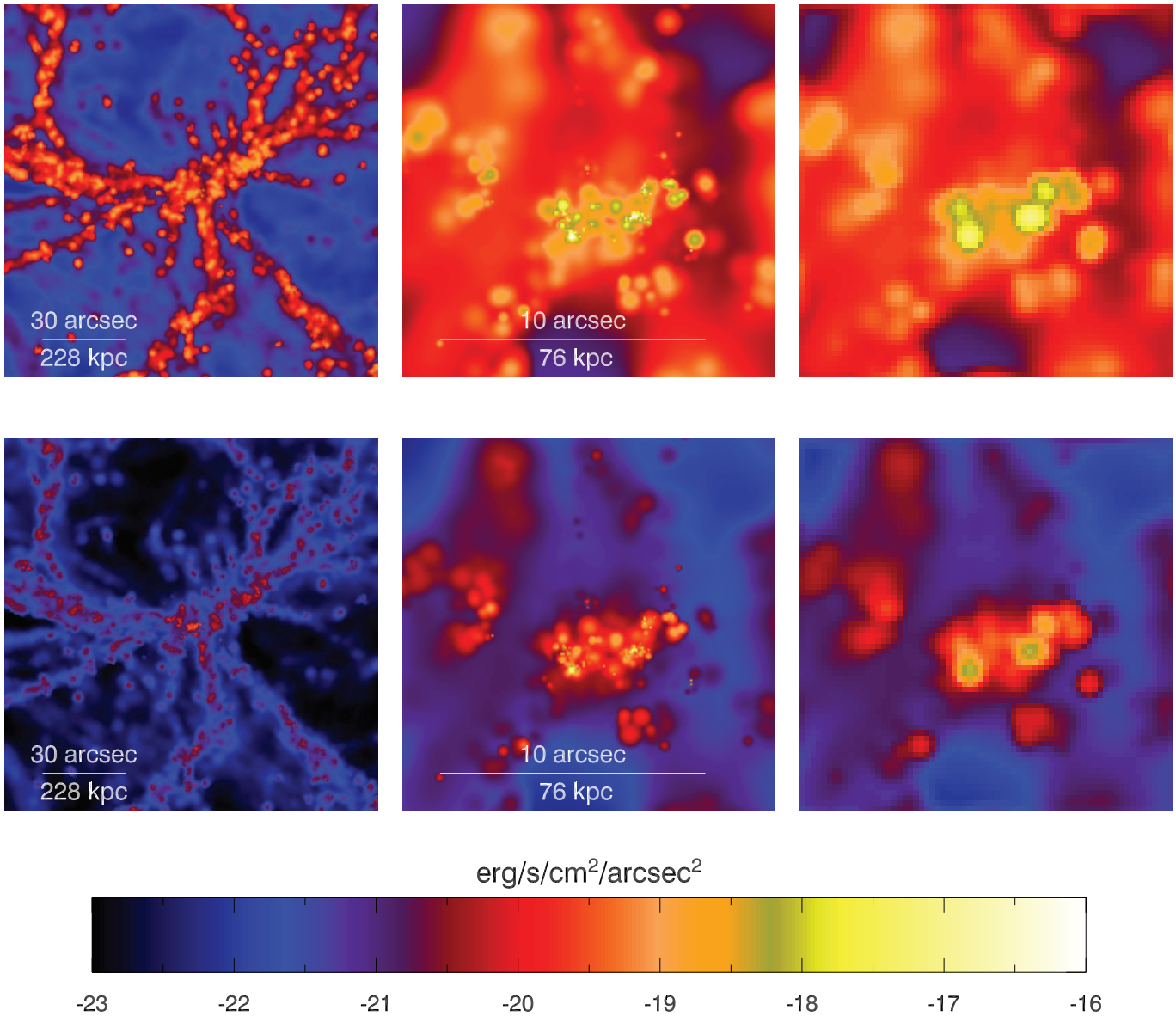

FIG. 3.—H I λ1216 (*top*) and He II λ1640 (*bottom*) cooling maps for the 11 Mpc simulation at $z = 3$. The line of sight depth is $\Delta z \simeq 0.019$. The left panels show a part ($\frac{1}{4} \times \frac{1}{4}$) of our simulation, the center panels show the brightest region at a finer pixel scale ($\sim$1.5 h^{-1} kpc per pixel), and the right panels show the cooling maps convolved with a 0.″5 FWHM Gaussian filter to mimic a typical ground-based observation (rebinned to 0.″2 pixel^{-1}). Note that we include Lyα and He II emission from the IGM assuming that the emissivity of the condensed phase is zero, the most conservative case. The Lyα cooling radiation from the gas around the forming galaxies will be observed as a diffuse and extended blob above $\sim 10^{-18}$ ergs s^{-1} cm^{-2} arcsec^{-2}, the current flux limit of ground-based detections ($R = 100$), whereas He II will be almost point-source–like at current detection limits.

temperature and density plots for the optically thin (optimistic) case. To make these phase diagrams, we extract temperature and density profiles for 100×100 evenly spaced lines of sight, apply our emissivities to each radial bin, and integrate the temperatures and densities with the H I λ1216 and He II λ1640 luminosities as weighting factors. Thus, each diagram represents the phases that we could actually probe by observing each line. In each phase diagram, the condensed phase of the IGM is delineated by dot-dashed lines. The sharp edge of the condensed phase at $T \sim 10^4$ K arises from the lack of metal-line cooling in our simulations. The diamonds in Figure 4 indicate the lines of sight that have He II λ1640 or H I λ1216 surface brightnesses larger than 10^{-19} ergs s^{-1} cm^{-2} arcsec^{-2}. Most He II λ1640 emission comes from a specific range of temperature ($10^5 < T < 10^6$) and density ($10^2 < \rho/\bar{\rho}_b < 10^3$) that is remote from the condensed phase, whereas the brightest H I λ1216 blobs have significant amounts of condensed phase gas. Because self-shielding becomes important in the condensed phase, we exclude this phase in calculating the cooling maps (in Fig. 3) to produce our most conservative predictions. As we expected, this cutoff does not affect the He II cooling maps seriously but does affect the H I λ1216 cooling map dramatically, as gas particles with $T < 10^{4.5}$ K cannot contribute to He II collisional excitation cooling but only to H I collisional excitation cooling. Therefore, our predictions for the He II λ1640 cooling radiation are far more robust than for H I λ1216.

The next factor that could modify the Lyα cooling maps is the radiative transfer of Lyα photons, which could alter the shapes and surface brightness profiles of the blobs substantially. Both the H I λ1216 and He II λ304 photons produced in the optically thick medium will be transported to the outer region by resonant scattering until the optical depth becomes smaller than $\tau \sim \frac{2}{3}$.

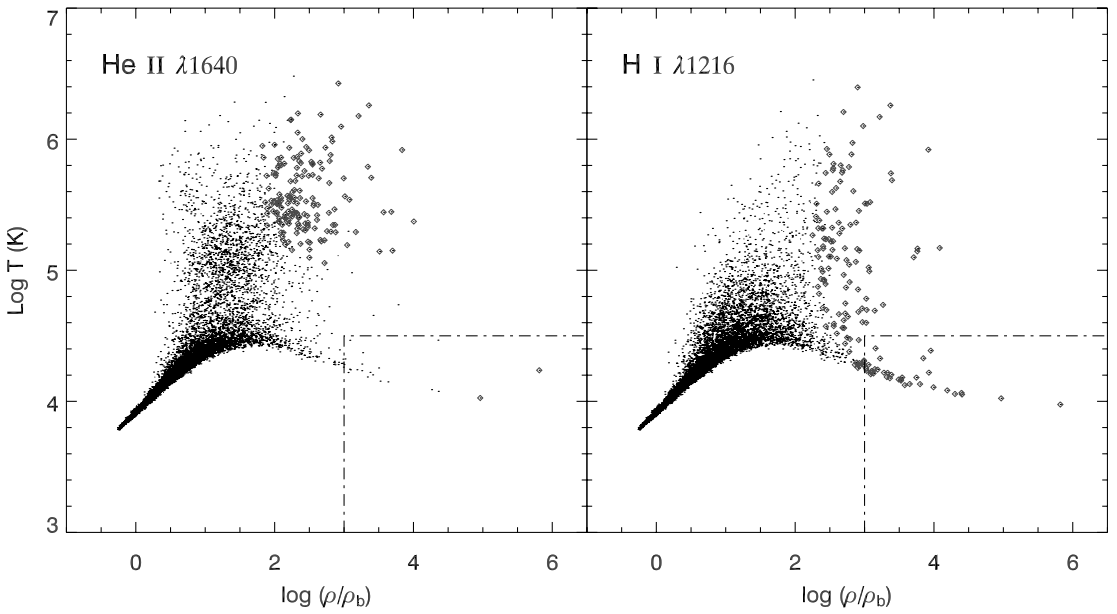

FIG. 4.—"Luminosity-weighted" phase diagram for 100×100 lines of sight through the simulation at $z = 3$ for He II λ1640 (*left*) and H I λ1216 (*right*). The diamonds indicate the lines of sight that have He II λ1640 or H I λ1216 surface brightnesses larger than 10^{-19} ergs s^{-1} cm^{-2} arcsec^{-2}. The condensed phase of the IGM ($T < 10^{4.5}$ and $\rho/\bar{\rho}_b > 10^3$) is represented by the dot-dashed lines. The brightest He II λ1640 blobs occupy a specific range of temperature ($10^5 < T < 10^6$) and density ($10^2 < \rho/\bar{\rho}_b < 10^3$), while the brightest H I λ1216 blobs tend to come from the high-density gas. Thus, the H I λ1216 cooling map is greatly affected by the condensed phase of the IGM. To be conservative, we thus exclude the condensed phase gas particles in generating the cooling maps (Fig. 3). [*See the electronic edition of the Journal for a color version of this figure.*]

Lyα photons escape eventually by scattering into the optically thin damping wing in the frequency domain, unless they are extinguished by dust. We expect that the IGM at $z \sim 3$ contains little dust and that the cooling emission from the IGM is sufficiently far from the star-forming regions, since we exclude the high-density gas particles in our condensed phase cut case. Therefore, the net effect of the resonant scattering in the spatial and frequency domains is to smooth the surface brightness out to the last scattering surfaces.

For example, Fardal et al. (2001) resorted to resonant scattering to explain the observed size of the Steidel blobs. However, owing to the complicated structure of the density and to turbulent velocity fields, it is difficult to predict how much radiative transfer blurs the surface brightness of the cooling blob. The large bulk motions will especially affect the transfer of Lyα photons. Depending on the optical depth and velocity field, photons can often undergo very little spatial diffusion and just random walk in velocity space until they reach a frequency where the optical depth is $\sim$1 (Zheng & Miralda-Escudé 2002). A Monte Carlo Lyα radiative transfer calculation would be an ideal tool to make more realistic spatial and frequency maps of Lyα cooling radiation (Zheng & Miralda-Escudé 2002; J. Kollmeier et al. 2006, in preparation).

In Figure 5, we show the profiles of density, temperature, velocity, and H I and He II emissivity for a line of sight toward a typical Lyα blob to illustrate the complicated structure of these quantities. Because we do *not* take into account these radiative transfer effects in our cooling maps, the H I λ1216 cooling map (Fig. 3, *top center*) should be smoothed to better represent reality. In contrast, because most He II resides in the ground state, making the IGM optically thin to the He II λ1640 line, our He II cooling maps should be accurate.

Besides gravitational cooling and photoionization caused by the UV background, supernova feedback is another energy source included in our simulations. When stars form in the simulations, supernova feedback energy is deposited into the surrounding gas

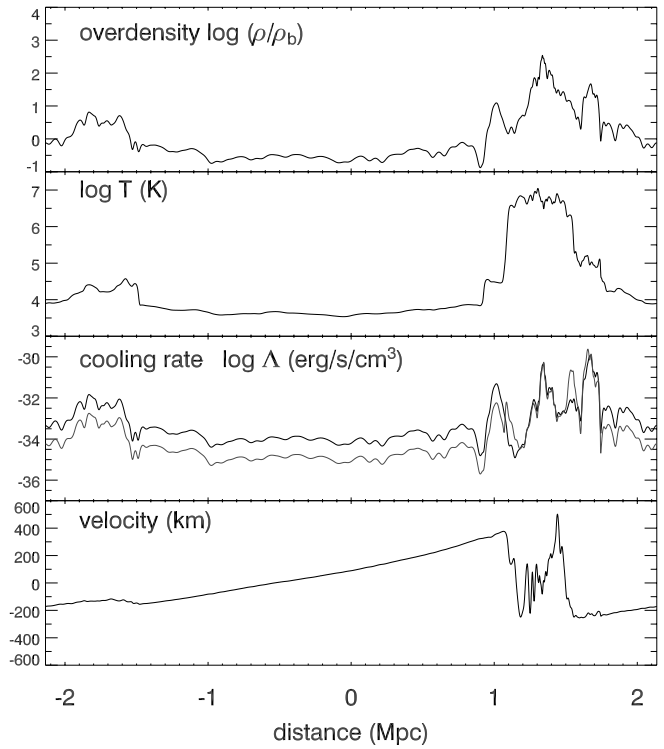

FIG. 5.—Profiles of density, temperature, H I λ1216 (*heavy*), and He II λ1640 (*light*) cooling rates, and velocity for a line of sight. Owing to the complicated structure of the density and the turbulent velocity fields, it is difficult to predict how much the radiative transfer blurs the surface brightness of Lyα cooling blobs. However, because the IGM is optically thin to He II, our He II cooling maps (Fig. 3) should be accurate. [*See the electronic edition of the Journal for a color version of this figure.*]

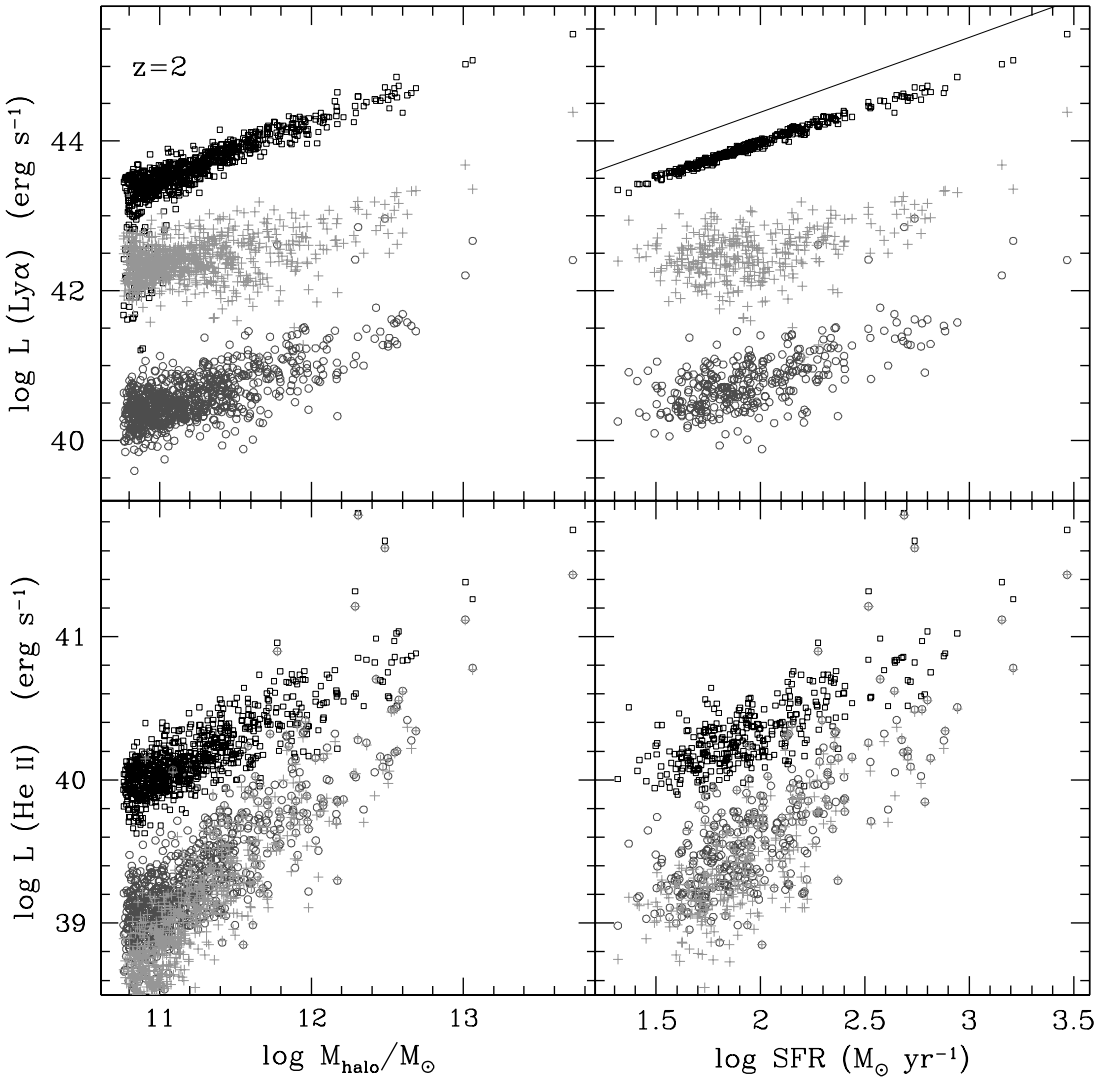

FIG. 6.—Lyα and He II luminosity as a function of the halo viral mass and the SFR in the 22 Mpc simulation at $z = 2$. The open squares, crosses, and circles represent the three different emissivity predictions: the optically thin case, the self-shielding correction case, and the condensed phase cut case, respectively. In the right panels we plot only blobs with a baryonic (star+gas) mass larger than 200 $m_{\rm SPH}$. Below this mass limit, the derived SFRs are not reliable owing to our limited resolution. As discussed in the text, Lyα luminosity changes dramatically depending on the prescription used for the self-shielded phase. The correlations between the cooling luminosity, halo mass, and SFR are as one generally expects: the more massive a galaxy is, the more gas accretes onto the galaxy, resulting in more cooling radiation and a higher SFR. The solid line in the top right panel represents the Lyα emission expected from star formation, assuming a conversion factor $f_{\rm Ly\alpha} = 2.44 \times 10^{42}$ ergs s^{-1} for a 1 $M_\odot$ yr^{-1} SFR with no dust absorption, no escaping ionizing photons, a Salpeter IMF, and solar metallicity. Note that under these assumptions the Lyα emission from star formation always dominates the cooling emission from the surrounding IGM. [*See the electronic edition of the Journal for a color version of this figure.*]

in the form of heat. Thermal energy deposited into dense, rapidly cooling gas is quickly radiated away, so feedback contributes somewhat to the cooling emission. However, we find that our density-temperature cutoff for the condensed phase effectively removes all the star-forming gas particles at each time step. Because the supernova thermal input is directly proportional to the star formation rate (SFR), our cooling maps without the condensed phase should not be seriously contaminated by supernova feedback energy. Thus, the cooling maps in Figure 3 with the condensed phase removed are still robust lower limits of the flux from the gravitational cooling. Fardal et al. (2001) also show that while the reradiated supernova energy dominates at lower luminosity, gravitational cooling becomes the dominant source as the mass and luminosity increase.

3.2. *Properties of Cooling Sources*

To study the properties of individual H I λ1216 and He II λ1640 sources like the ones shown in the cooling maps, we identify discrete groups of gas particles associated with individual dark matter halos and then calculate the total Lyα and He II λ1640 luminosities for these sources. To find the dark matter halos, we apply a friends-of-friends algorithm with a linking length that is 0.25 times the mean interparticle separation. We count a gas particle as a member of the source, i.e., blob, associated with the dark matter halo if the distance from the potential center is less than the virial radius of the halo. We then add the Lyα and He II λ1640 luminosities of the particles to obtain the total cooling luminosities of the blob. We restrict our analysis to blobs with more than 64 gas particles and 64 dark matter particles to mitigate numerical resolution effects. Thus, the smallest halo in the 22 Mpc simulation has a gas mass of $M_{\rm gas} = 6.3 \times 10^9\ M_\odot$ and dark matter mass of $M_{\rm dark} = 5.0 \times 10^{10}\ M_\odot$. These masses decrease to $M_{\rm gas} = 8.5 \times 10^8\ M_\odot$ and $M_{\rm dark} = 6.8 \times 10^9\ M_\odot$ in the 11 Mpc simulation.

The H I λ1216 and He II λ1640 cooling luminosities show tight correlations with halo mass and SFR (Fig. 6). The open squares,

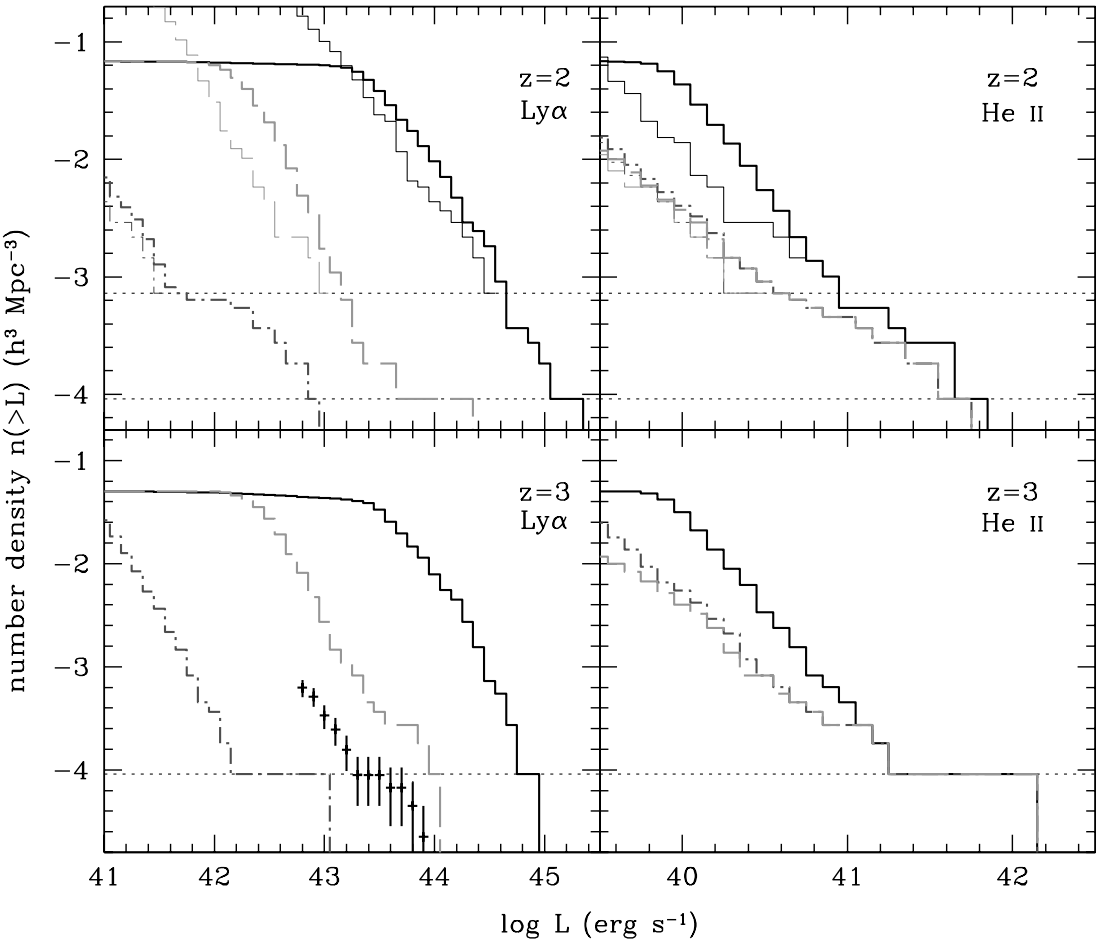

FIG. 7.—LFs of Lyα and He II λ1640 cooling radiation at $z = 2$ (*top*) and 3 (*bottom*). The solid, dashed, and dot-dashed lines represent the optically thin, the self-shielding correction, and the condensed phase cut cases, respectively. In the top panels, for each emissivity case, the LFs from the 11 Mpc and 22 Mpc simulations are denoted with light and heavy lines, respectively. The horizontal dotted lines indicate the number density of one halo in the 11 Mpc and 22 Mpc simulations. Note that the 22 Mpc results extend to higher luminosity than the 11 Mpc results and that even the larger simulation may underestimate the density of high-luminosity systems. In the bottom panels, we show only results from the 22 Mpc simulation. For comparison, we show the LF of the Subaru Lyα blob sample (*crosses*; Matsuda et al. 2004). The Subaru Lyα blobs could arise from a variety of mechanisms (see text), including cooling radiation. It is suggestive, however, that their LF lies between our predictions for the self-shielding correction and condensed phase cut cases. Note also that the Lyα LF is very sensitive to the assumed emissivities, whereas the He II λ1640 cooling luminosity depends much less on the treatment of the self-shielded or condensed phase of the IGM. [*See the electronic edition of the Journal for a color version of this figure.*]

crosses, and circles in this figure represent the luminosities for the three different emissivities discussed in § 2.2: the optically thin case, the self-shielding correction case, and the condensed phase cut cases, respectively. The correlations are as one would expect: the more massive a galaxy is, the more gas accretes onto the galaxy, resulting in more cooling radiation and a higher SFR. The distribution of cooling luminosity is continuous, and we do not find any evidence that extended Lyα or He II emission originates only from high-mass systems or high-density regions.

The solid line in the top panel in Figure 6 indicates the Lyα emission due to recombination from stellar ionizing photons. We assume a conversion factor of $f_{\mathrm{Ly}\alpha} = 2.44 \times 10^{42}$ ergs s^{-1} for a 1 $M_\odot$ yr^{-1} SFR with no dust absorption, no escaping ionizing photons, a Salpeter IMF, and solar metallicity. Under these assumptions the Lyα emission from star formation in galaxies always dominates the Lyα emission from the surrounding IGM, even in the (most optimistic) optically thin case. This result is consistent with the predictions of Fardal et al. (2001) and Furlanetto et al. (2005).[2]

[2] In contrast, we do not find the trend of Fardal et al. (2001) in which Lyα from cooling radiation dominates the Lyα from star formation in more massive systems. We suspect that this difference is a consequence of including a photoionizing background in the simulation analyzed here.

The strong correlation between the Lyα cooling rate in the optically thin case (*squares*) and the SFR results from the fact that the gas in the condensed phase tends to satisfy the star formation criteria of the simulation and is likely to form stars in the next time step. In contrast, the He II emission caused by star formation is quite uncertain because only extremely low metallicity ($Z < 10^{-5}$) stars can emit the hard ionizing photons necessary to ionize He II. However, star formation at $z = 2$–3 is unlikely to be dominated by Population III or extremely low metallicity stars. Unlike for Lyα, the contribution of star formation to He II must be negligible. We discuss this point in more detail in § 4.

Figure 7 shows the Lyα and He II luminosity functions (LFs) for the three emissivity cases at $z = 2$ and 3. The LFs include emission only from the IGM. The solid, dashed, and dot-dashed lines represent the optically thin, the self-shielding correction, and the condensed phase cut cases, respectively. The horizontal dotted lines indicate the number density of one halo in the simulation volume. Note that because the larger simulations contain higher mass systems, the distributions extend to brighter blobs as we increase the simulation volume. Note also that the Lyα luminosity function is very sensitive to the assumed emissivities, whereas the He II λ1640 cooling luminosity depends

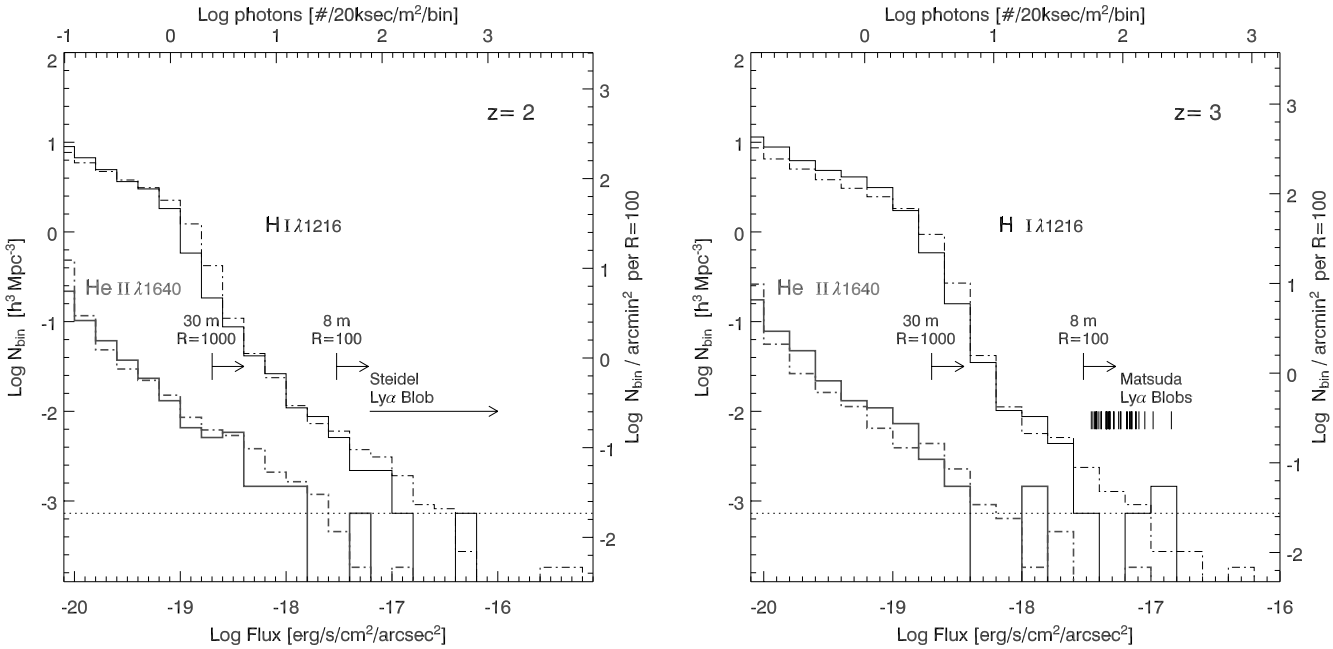

FIG. 8.—Distributions of surface brightnesses in the cooling maps for the IGM at $z = 2$ and 3. Heavy and light solid lines represent the surface brightness histograms of rebinned ($0\farcs5 \times 0\farcs5$) pixels for He II λ1640 and H I λ1216, respectively, in the 11 Mpc simulation. We show the S/N > 5 detection limits for a 30 hr observation with an 8 m telescope and $R = 100$ narrowband filter, and with a 30 m telescope and $R = 1000$ filter. The right y-axis represents the number of binned pixels per square arcminute per the redshift width for the $R = 100$ filter. The dotted lines at the bottom of each panel indicate one detection in the simulation. The dot-dashed lines represent the surface brightness distributions for the 22 Mpc simulation. Detection of the brightest H I λ1216 and He II λ1640 blobs at $z = 2$ and 3 is possible with deep narrowband imaging on a 6–8 m class telescope. Note that the larger simulation extends the bright tail of the surface brightness distribution. Even larger simulation volumes might therefore predict still brighter, thus more easily detectable, systems. [*See the electronic edition of the Journal for a color version of this figure.*]

much less on the treatment of the self-shielded or condensed phase of the IGM. This large variation of the Lyα luminosity is consistent with the results of Furlanetto et al. (2005).

3.3. *Detectability and Observational Strategy*

To estimate the detectability of cooling emission from the extended sources, we convert the rest-frame cooling maps at $z = 2$ and 3 into observed surface brightness maps and rebin them with a pixel scale of $0\farcs5 \times 0\farcs5$ to mimic the independent resolution elements of ground-based observations (Fig. 3). Figure 8 shows the surface brightness distributions of the rebinned cooling maps at $z = 2$ and 3, assuming the conservative condensed phase cut case. Note that the distributions depend strongly on the size of the bins in the surface brightness maps, because the bright, small-scale structures are smoothed out by binning. We express each surface brightness distribution in terms of the number of binned pixels per comoving volume and also the number of pixels per square arcminute if one were to observe through a $R = 100$ narrowband filter. The projected angular extents of the 11 Mpc simulation at $z = 2$ and 3 are $11\farcm4$ and $9\farcm4$, respectively. The depth of the 11 Mpc simulation is $\Delta z \simeq 0.013$ and 0.019 for $z = 2$ and 3, respectively.

Deep, wide-field ($\sim 30' \times 30'$), narrowband ($R > 100$) imaging is an effective way to detect cooling radiation, because sky noise dominates in this low surface brightness range. For example, the average sky background at 6500 Å on the ground is $\sim 10^{-17}$ ergs s^{-1} cm^{-2} arcsec^{-2} Å^{-1}, comparable to our estimates for the brightest blobs. In Figure 8, we show the 5 σ detection limits for typical $R = 100$ narrowband imaging with an 8 m class telescope and for $R = 1000$ imaging with a hypothetical 30 m telescope. We assume a peak system throughput of $\sim$35%, a Mauna Kea sky background (for the 50% dark condition), and a 30 hr exposure time. We estimate the signal-to-noise ratios (S/N's) for one binned pixel ($0\farcs5 \times 0\farcs5$), which corresponds to $\gtrsim 2 \times 2$ instrumental pixels in ground-based CCD detectors.

3.3.1. H I λ1216

We predict that H I λ1216 cooling emission from the brightest blobs at $z = 2$ and 3 is detectable by 6–8 m class telescopes with moderate resolving power ($R = 100$). The limiting sensitivity of current surveys for high-z Lyα emitters is $\sim 10^{-18}$ ergs s^{-1} cm^{-2} (e.g., Malhotra & Rhoads 2004 and references therein). It is encouraging that even our most conservative predictions suggest that the Lyα blobs arising from gravitational cooling radiation are detectable with a reasonable amount of telescope time.

The Lyα surface brightness of the largest system in our $z = 3$ simulation ($M_{\rm halo} \sim 6.5 \times 10^{12}\ h^{-1}\ M_\odot$), corresponding to the brightest blob in Figure 3, is consistent with the *mean* surface brightnesses of the Lyα blobs of the Matsuda et al. (2004) sample (represented with small vertical bars in the Fig. 8). Note that our predicted Lyα blob luminosities depend on the different emissivities for the self-shielded phase and/or the exact location of our density-temperature cut of the condensed phase. Though the surface brightnesses of the predicted and observed blobs are consistent, the *luminosity* of our brightest Lyα blob is fainter than that of observed blobs (see Fig. 7), possibly because of our conservative assumptions for the self-shielded phase.

3.3.2. He II λ1640

A pixel-by-pixel comparison of the H I λ1216 and He II λ1640 cooling maps reveals that without the condensed phase, the He II λ1640 flux is always $\gtrsim$10 times fainter than that of H I λ1216. The He II λ1640 emission could be 1000 times fainter than Lyα in the optically thin case, i.e., the most optimistic Lyα

prediction. Nonetheless, detection of the He II λ1640 cooling line from $z = 2$ sources is clearly feasible with 6–8 m class telescopes and even possible at $z = 3$. Though the number statistics of bright blobs are limited by the relatively small volume of our simulations, we expect one source in the 11 Mpc simulation and six sources in the 22 Mpc simulation at $z = 2$ with areas of $\gtrsim 0\farcs5 \times 0\farcs5$ above the surface brightness detection threshold of $\sim 5 \times 10^{-18}$ ergs s^{-1} cm^{-2} arcsec^{-2} ($R = 100$; Fig. 8, *arrow*).

Thus, the space density of the sources from which we could detect not only Lyα but also He II λ1640 emission with narrowband imaging corresponds to a comoving number density of $\sim(5\text{–}7) \times 10^{-4}\ h^3$ Mpc^{-3} or $\sim$0.02 arcmin^{-2} per $R = 100$ filter ($\Delta z = 0.03$; $\Delta\lambda \simeq 49$ Å for He II λ1640).

If we consider the larger survey volume typically accessible by modern narrowband imagers, we could expect better survey efficiency than that described above. Because cosmological simulations do not contain power on scales larger than their finite sizes, the largest objects in the simulation are typically underestimated in number and size. For example, the luminosity functions and surface brightness distributions in Figures 7 and 8 extend their bright limits as the volume of the simulation increases. Therefore, one might expect to detect even brighter blobs by surveying more volume. For example, many current wide-field imagers and spectrographs have half-degree fields of view, so it is possible to survey a volume $\sim$17 times larger than that encompassed by our 11 Mpc simulation at $z = 2$ (or a volume about twice that of the 22 Mpc simulation). Therefore, if we naively extrapolate the number of detectable He II sources in our 11 Mpc and 22 Mpc simulations, then 17 ($\pm$17) and 13 ($\pm$5) He II sources would be detected, respectively. The numbers within parentheses indicate Poisson errors.

Our results predict that bright He II sources are always bright Lyα cooling blobs. Observationally, the difficulties in searching for He II cooling sources could be eased (1) by pursuing narrowband Lyα imaging first, detecting Lyα blobs, and looking for He II λ1640 emission in those blobs with follow-up observations or (2) by adopting a combined multislit spectroscopy+narrowband filter approach (Martin & Sawicki 2004; Tran et al. 2004) to identify Lyα blobs (which can then be targeted for He II).

The latter technique is potentially quite effective despite the faint surface brightness of the Lyα and He II blobs. This technique employs multiple parallel long slits with a narrowband filter that limits the observed spectral range to a few hundred angstroms and, by dispersing the sky background, achieves better sensitivity than narrowband imaging alone. In the sense that this technique trades off survey volume (or sky coverage) to go deeper in flux, it is about as efficient as simple narrowband imaging for surveys of Lyα emitters, which are not as extended as Lyα blobs. However, the multislit window technique is superior to narrowband imaging for low surface brightness objects like the Lyα and He II blobs discussed here. It has the further advantages that (1) it provides the spectral and kinematic data necessary to distinguish the origins of blob emission (§ 4) and (2) it enables us to exclude contaminating emission lines, such as Hα, Hβ, [O III], and [O II], from nearby star-forming galaxies by measuring the line shapes (e.g., line asymmetries and line doublets) and blueward continuum. If this technique is employed with large field-of-view imagers, the survey volume covered by the multiple slits is still reasonably large ($\sim$10% of the whole field of view).

It is possible to search for He II cooling radiation at lower redshifts than $z \sim 2$–3. For example, $z \approx 1.5$ is the lowest redshift at which He II λ1640 still lies at an optical wavelength ($\lambda_{\rm obs} \approx 4100$ Å). Because metal abundances in the IGM do not change very much over $z \sim 2$–4 (Schaye et al. 2003), it is unlikely that our basic assumption of a primordial composition (§ 2) is violated seriously at $z \approx 1.5$. Any blind search for He II λ1640 blobs at $z = 1.5$–2 will be contaminated by H I Lyα emission from $z \approx 3$ sources if only one emission line is identified in the spectrum. In this case, the blob's redshift could be further constrained by obtaining a redshift for the galaxy it surrounds.

He II λ1640 cooling radiation at very low redshifts ($z \lesssim 0.5$) is potentially detectable in the ultraviolet using UV satellites or *HST*. For example, Furlanetto et al. (2003) show that the detection of the bright cores of H I λ1216 emission from $z \lesssim 0.5$ sources is feasible with deep wide-field UV imaging, e.g., with *The Galaxy Evolution Explorer* (GALEX) or the proposed *Space Ultraviolet-Visible Observatory* (*SUVO*; Shull et al. 1999). Because H I λ1216 and He II λ1640 trace different phases of the gas, as shown in Figure 4, combined observations of these two lines, e.g., of their morphologies and line ratios, would probe different phases of the IGM.

3.3.3. He II λ304

In contrast to H I λ1216 and He II λ1640, He II λ304 photons redshifted to wavelengths shorter than the photoionization edge of H I and He I (912 and 504 Å, respectively) can be absorbed by neutral hydrogen and neutral helium. Even if they escape the blobs, He II λ304 photons are removed from the line of sight owing to cumulative absorption by the intervening neutral IGM, including the Lyα forest and damped Lyα systems. We estimate the transmission of He II λ304 through the intervening IGM using Monte Carlo simulations as described in Møller & Jakobsen (1990) with the updated statistics of Lyman forest and Lyman limit systems (i.e., number density evolution and column density distribution) from Jakobsen (1998). For the emitters at $z = 3$, we find that the transmission factor averaged over all lines of sight is $\sim$12% and that 67% (76%) of the sight lines will have transmission lower than 1% (10%). Therefore, though the He II λ304 emissivity is roughly 10 times higher than that of He II λ1640 (Fig. 1 in § 2.1), we expect the He II λ304 cooling map to be fainter than that of He II λ1640 in most cases and to vary strongly from sight line to sight line.[3]

He II λ304 photons can also be destroyed by the H I and He I inside the blobs, because He II λ304 photons experience a large number of scatterings before escaping. The destruction probability by H I and He I atoms per scattering is given by

$$\epsilon = \frac{n_{\rm H\,I}\sigma_{\rm H\,I} + n_{\rm He\,I}\sigma_{\rm He\,I}}{n_{\rm H\,I}\sigma_{\rm H\,I} + n_{\rm He\,I}\sigma_{\rm He\,I} + n_{\rm He\,II}\sigma_{\rm Ly\alpha}}, \qquad (3)$$

where $\sigma_{\rm H\,I}$ and $\sigma_{\rm He\,I}$ are the photoionization cross sections of H I and He I at 304 Å, respectively, and $\sigma_{\rm Ly\alpha}$ is the integrated scattering cross section of He II λ304. The abundances of H I and He I atoms are smaller than for He II, and their photoionization cross sections are also much smaller than the resonant cross section of He II λ304, by a factor of $\lesssim 2 \times 10^{-5}$. We estimate that the destruction probability is $\epsilon \gtrsim 5 \times 10^{-8}$ at a temperature of $T \sim 10^{4.8}$ without applying the self-shielding correction. In the self-shielded regions where more neutral hydrogen can reside, this probability rises. Thus, the escape probability of an He II λ304 photon from a blob is $f_{\rm IGM} \simeq (1 - \epsilon)^{N_\tau}$, where $N_\tau \simeq \tau^2$ is the number of scatterings required to escape the blob, if it is

[3] If one sight line does not have any Lyman limit or damped Lyα systems, it will have $\sim$87% transmission on average due only to Lyman forest systems.

approximated by an optically thick slab. For example, we obtain $f_{\rm IGM} \simeq 0.7\%$ for $\tau_{\rm He\,II} = 10^4$. Therefore, we cannot ignore the absorption by H I and He I atoms in the high density gas. However, the number of scatterings N_τ is very difficult to estimate correctly because of the complex density and velocity structure of the blob, unless one carries out full three-dimensional hydroradiative transfer calculations (which are beyond the scope of this paper). For certain geometries and velocity fields, bulk motions of the gas will help the He II λ304 photons escape the blob with fewer scatterings (e.g., Zheng & Miralda-Escudé 2002).

Owing to intervening absorption and the destruction inside the blobs, He II λ304 is the most uncertain cooling line we consider. Although He II λ304 is diminished significantly by the intervening IGM, if the escape fraction from the IGM is significant ($f_{\rm IGM} \simeq 1$), the detection of He II λ304 may not be out of the question with a large-aperture UV/optical-optimized space telescope (e.g., *SUVO*; Shull et al. 1999). An advantage of observing He II λ304 in the far-ultraviolet in space is that the sky background is very low ($\sim 10^{-23}$ ergs s^{-1} cm^{-2} arcsec^{-2} Å^{-1} at 1250 Å) compared to the optical ($\sim 10^{-18}$ ergs s^{-1} cm^{-2} arcsec^{-2} Å^{-1} at 6500 Å), except for the geocoronal emission lines (e.g., Lyα λ1216 and O I λ1304). Thus, if these geocoronal emission lines can be eliminated with blocking filters or by adopting an L2 orbit, the direct detection of He II λ304 is feasible. In this case, the detector noise—especially the dark current—will dominate. Recent developments in UV detector technology are very promising, so the possibility of studying these blobs at those wavelengths remains open.

4. DISCUSSION

Until now, we have only considered the cooling radiation from gas that is losing its gravitational energy, falling into a galaxy-sized dark halo, and ultimately forming stars. Photoionization by these stars is another possible heating source for the blobs. Starburst-driven superwinds or active galactic nuclei (AGNs), which are not included in our simulations, are other potential blob energy sources (e.g., see the discussions in Steidel et al. 2000; Matsuda et al. 2004). Although the radiation from gas heated by these feedback processes is not generally termed "cooling radiation," the energy injected into the surrounding gas can also be released through line emission. Thus, our estimates for cooling emission might be lower limits for the actual fluxes in the cooling lines. In this section, we assess whether other H I λ1216 and He II λ1640 sources overwhelm our gravitational cooling signals and then discuss how to discriminate among these other possible mechanisms in order to use H I λ1216 and He II λ1640 cooling lines to study gas infall into galaxies.

4.1. *Photoionization by Stellar Populations*

UV photons from massive stars in a galaxy or blob ionize the surrounding interstellar medium, and the recombination lines from these nebulae could contribute to the Lyα and He II line fluxes. Generally, the recombination line luminosity is proportional to the SFR and is given by

$$L_{\rm line} = e^{-\tau_{\rm dust}}(1 - f_{\rm esc}) f_{\rm IGM} f_{\rm line} \left(\frac{\rm SFR}{M_\odot\ {\rm yr}^{-1}} \right), \qquad (4)$$

where $\tau_{\rm dust}$ is the dust optical depth for the ionizing continuum in the interstellar medium (ISM), $f_{\rm esc}$ is the fraction of ionizing photons that escape the star-forming galaxy, $f_{\rm IGM}$ is the fraction of photons that escape the surrounding IGM, and $f_{\rm line}$ is the conversion factor from the SFR to the line luminosity in ergs per second. This SFR conversion factor depends on the metallicity, initial mass function (IMF), and evolutionary history of the stars in the blobs (e.g., a lower metallicity and a top-heavy IMF produce more ionizing photons and thus more recombination line photons).[4]

The conversion factor for H I λ1216, f_{1216}, is large enough to make it difficult to distinguish the cooling lines (of IGM origin) from the recombination-induced lines (of ISM origin). For example, Schaerer (2003) finds $f_{1216} = 2.44 \times 10^{42}$ ergs s^{-1} for a constant star formation history, solar metallicity, and a Salpeter IMF with a mass range of 1–100 $M_\odot$. Thus, for an SFR $= 10\ M_\odot$ yr^{-1}, $f_{\rm esc} \simeq 0.1$, $e^{-\tau_{\rm dust}} \simeq 0.1$, and $f_{\rm IGM} \simeq 1$, we obtain the observed flux, $F_{1216} \simeq 2.9 \times 10^{-17}$ ergs cm^{-2} s^{-1}, due to the stars in a Lyα blob at $z = 3$, which is comparable to the surface brightness of the brightest blobs in our simulations (see § 3.3 for the blob luminosity functions). Therefore, the contamination of the H I λ1216 line by stars is not negligible, unless the Lyα photons from star-forming regions are heavily absorbed by a dusty ISM (e.g., in highly obscured submillimeter galaxies or LBGs with the damped Lyα absorption). Because Lyα cooling radiation is produced sufficiently far from the star-forming region and thus should be less susceptible to dust attenuation than the Lyα emission from the stellar populations, it might be possible to isolate extended Lyα cooling radiation in these galaxies.

However, in the case that Lyα photons emitted by stars escape the galaxy (e.g., Lyα emitters), it will be challenging to distinguish the Lyα cooling radiation from the Lyα produced by the stellar populations unless the various parameters, such as $f_{\rm esc}$, $f_{\rm IGM}$, and SFR, are fully constrained.

In contrast, He II λ1640 emission appears to be limited to very small metallicities [$\log(Z/Z_\odot) \lesssim -5.3$] and Population III objects, because stars of solar or subsolar metallicities emit few if any He II ionizing photons (Bromm et al. 2001; Schaerer 2003; Tumlinson et al. 2003). Using He II λ1640 to detect the first hard-ionizing sources, such as metal-free stellar populations, the first miniquasars, or even stellar populations before the reionization epoch, has been proposed (e.g., Tumlinson et al. 2001; Oh et al. 2001; Barton et al. 2004). In this paper, we take advantage of this fact to discount the contributions of stellar populations to the He II λ1640 cooling line. Even for $Z = 10^{-5}$, $f_{1640} = 1.82 \times 10^{40}$ ergs s^{-1} ($\simeq 6 \times 10^{-4} f_{1216}$) for an extremely top-heavy IMF containing only stars in the range 50–500 $M_\odot$ (and the O and B stars of solar or subsolar metallicities in local star-forming galaxies produce nebular He II λ1640 emission at least an order of magnitude smaller; Schaerer 2003). For the same assumptions used in the Lyα calculation above, we obtain an observed flux of $F_{1640} \simeq 2.2 \times 10^{-19}$ ergs cm^{-2} s^{-1} from the blob stars at $z = 3$, an order of magnitude below the brightest He II λ1640 blobs in our simulations. Therefore, it is very unlikely that the He II λ1640 photons originating from stars contaminate the gravitational cooling emission, unless significant numbers of metal-free stellar populations are forming. Thus, He II λ1640 cooling radiation is much less contaminated than H I λ1216 by recombination lines originating from star-forming galaxies.

[4] Note that the eq. (4) does *not* take into account the dust absorption of Lyα photons by ISM after Lyα photons escape from the H II region. When the H I optical depth in the ISM is high enough, Lyα photons will experience a large number of resonant scatterings before escaping the galaxy. These scatterings will increase the effective dust optical depth and destroy Lyα photons preferentially. However, the actual optical depth is likely to strongly depend on the kinematics of neutral gas and the geometry of the galaxy, which are hard to quantify.

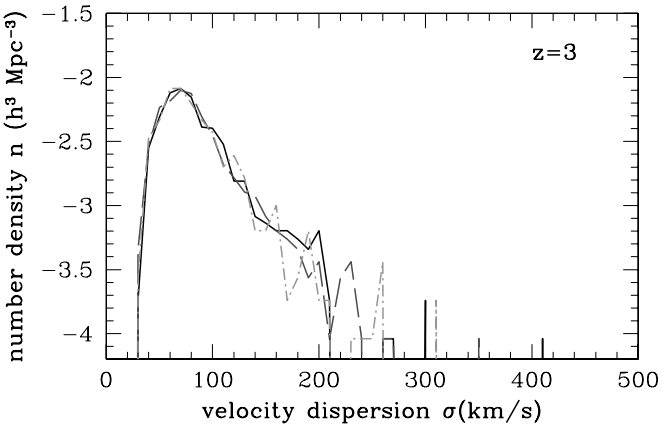

FIG. 9.—Distribution of He II λ1640 flux-weighted velocity dispersion of the gas particles associated with individual dark matter halos. The different lines represent the velocity dispersions in the *x*-, *y*-, and *z*-directions. Note that the velocity dispersion due to gas accretion is less than 400 km s^{-1}, in contrast to the typical galactic wind speed of ~400–800 km s^{-1} (Heckman et al. 2000). Thus, the width of the optically thin He II λ1640 line could be used as a diagnostic to discriminate between the galactic wind and the gravitational cooling hypotheses for powering Lyα blobs. [*See the electronic edition of the Journal for a color version of this figure.*]

The only caveat is the possibility of He II λ1640 emission arising not from stars directly, but from the hot, dense stellar winds of W-R stars, the descendants of O stars with masses of $M > 20$–$30\ M_\odot$. W-R populations formed in an instantaneous starburst at high redshifts would not seriously contaminate the He II λ1640 cooling radiation, because W-R stars are very short-lived (≲3 Myr) and their number relative to O stars (W-R/O) drops as the metallicity decreases below solar. In the case of continuous star formation, a stellar population synthesis model (Starburst99; Leitherer et al. 1999) predicts that the maximum number of W-R stars is reached ~10 Myr after the initial burst. Using the He II λ1640 luminosity of a W-R star (Schaerer & Vacca 1998) and the number evolution of W-R stars from Starburst99 under the assumptions of a Salpeter IMF (1–100 $M_\odot$), subsolar metallicity ($Z \leqslant 0.4\ Z_\odot$), and a massive SFR of 100 $M_\odot$ yr^{-1} over at least 10 Myr, we estimate the He II λ1640 line luminosity due to W-R stellar winds to be $\lesssim 10^{42}$ ergs s^{-1}. Although this He II λ1640 luminosity is comparable to the predicted He II cooling radiation, it is possible to discriminate between the two He II λ1640 sources in individual objects because the emission from W-R winds should be much broader (e.g., ~1000 km s^{-1}; see Fig. 9 in § 4.3, which is relevant here even though it is presented in the context of the galactic superwind scenario).

One way to test our predictions in this section is to look more closely at the He II λ1640 emission associated with high-redshift star-forming galaxies, i.e., the LBGs with vigorous SFRs. Shapley et al. (2003) show that composite spectra of LBGs have very broad (FWHM ~ 1500 km s^{-1}) He II λ1640 profiles regardless of their Lyα emission strength. While they attribute the He II features to W-R stellar winds, Shapley et al. have difficulty reproducing the strength of the He II lines using stellar population synthesis models with reasonable parameters. Because of this inconsistency, we speculate that some fraction of the He II features may come from the cooling of gas falling into these galaxies along line of sight. It would be worthwhile to obtain high S/N spectra of individual LBGs and their surroundings to see if the He II line is present, especially outside the galaxy, and relatively narrow.

4.2. *Photoionization by AGNs*

AGNs inside the star-forming regions of blobs could photoionize the surrounding gas and generate He II λ1640 as well as H I λ1216 emission. The predicted size (a few arcseconds) and surface brightness (~10^{-18} to 10^{-16} ergs s^{-1} cm^{-2} arcsec^{-2}) of an extended Lyα blob enshrouding a quasar are consistent with the observed quantities (Haiman & Rees 2001).

How many AGN-powered sources might we expect in a Lyα/He II blob survey? Unfortunately, it appears that there is no easy way to predict Lyα/He II luminosity from the surrounding IGM, because we do not know how much neutral IGM is distributed around the AGN. Therefore, we take a conservative approach to estimate the number of the AGN-powered sources. First, we establish a simplistic relationship between the induced Lyα (or He II) blob luminosity and the X-ray luminosity of the AGN, then we estimate the number of AGN-powered blobs based on the known hard X-ray luminosity function of AGNs at $z = 2$–3. If there are not many relative to the number of blobs powered by gravitational cooling radiation, then we could conclude that they are unlikely to complicate the interpretation of extended Lyα/He II sources.

We assume that all the ionizing photons from an AGN with a simple power-law spectrum, $L_\nu = L_0(\nu/\nu_0)^\alpha$, are absorbed by the surrounding medium and re-emitted as recombination lines. The line (Lyα or He II) luminosity of the surrounding blob is then given by

$$L_{\rm line} = c_{\rm line} Q = c_{\rm line} \int_{\nu_{\rm LL}}^{\infty} \frac{L_0}{h\nu} \left(\frac{\nu}{\nu_0}\right)^{\alpha}, \qquad (5)$$

where Q is the number of ionizing photons emitted per unit time, $\nu_{\rm LL}$ is the frequency of the Lyman limits for the hydrogen and He II ($h\nu_{\rm LL} = 13.6$ and 54.4 eV, respectively), and the line-emission coefficient $c_{\rm line}$ in ergs is the energy of the line photon emitted for each H I or He II ionizing photon. For case B recombination with an electron temperature of $T_e = 30{,}000$ K and an electron number density of $n_e = 100$ cm^{-3}, we obtain $c_{1216} = 1.04 \times 10^{-11}$ and $c_{1640} = 5.67 \times 10^{-12}$ ergs (see Schaerer 2003). We adopt a spectral index $\alpha = -1.8$ for the extreme UV (Telfer et al. 2002) and assume that this α is valid even in the X-ray. The hard X-ray luminosity of AGN ($L_{\rm X}$) is simply given by the integration of L_ν between 2 keV and 8 keV.

Once the Lyα (or He II) luminosity is monotonically linked with the AGN X-ray luminosity, we estimate the number density of AGN-powered sources from the hard X-ray luminosity function (e.g., Barger et al. 2003; Cowie et al. 2003). To power a blob with $L_{\rm Ly\alpha} = 10^{43}$ ergs s^{-1}, an AGN must have $L_{\rm X} \gtrsim 10^{41.8}$ ergs s^{-1}, which would generate an He II blob with $L_{\rm He\,II} \gtrsim 10^{41.7}$ ergs s^{-1}. Around the required X-ray luminosity, Cowie et al. (2003) derive the number density of X-ray–selected AGNs regardless of their optical AGN signatures to be $1.3 \times 10^{-5} \lesssim \Phi(L_{\rm X} > 10^{42}$ ergs s$^{-1}) \ll 1.4 \times 10^{-4}$ Mpc^{-3} at $2 < z < 4$. The extreme upper limit was determined by assigning all the unidentified sources in the survey to $2 < z < 4$ and is thus very conservative. For the brightest cooling sources in our simulations (Fig. 7), we find $\Phi(L_{\rm Ly\alpha} \gtrsim 10^{43}) \sim 3 \times 10^{-5}$ Mpc^{-3} and $\sim 9 \times 10^{-4}$ Mpc^{-3} for the condensed phase cut and the self-shielding correction cases, respectively.[5] Note again that our assumption that all the ionizing photons from all AGNs are absorbed to produce Lyα/He II photons is very conservative and that we are clearly overpredicting the number of AGN-powered blobs. However, even under this conservative assumption the number density of AGN-powered sources is only marginally comparable to the number density of cooling

[5] The number density of Lyα blobs [of unknown origin(s)] from the Subaru survey (Matsuda et al. 2004) lies between these two cases.

sources in our simulations. Therefore, at present, we conclude simply that a survey for extended Lyα and He II cooling radiation is not likely to be swamped by AGN-powered sources.

The above arguments are statistical, whereas distinguishing gravitational cooling radiation from the emission of AGN-photoionized gas for an *individual* source requires a multiwavelength approach. It is therefore useful to target fields with a large amount of ancillary data (e.g., deep broadband or X-ray imaging) to make an unambiguous detection of a true He II cooling blob. First, searching for the C IV (1549 Å) emission line in the optical spectrum of the source is a good way to identify an AGN (e.g., Keel et al. 1999). The composite spectra of optically selected quasars show bright C IV lines, but much fainter He II lines (Telfer et al. 2002). The recently discovered Lyα blob associated with a luminous mid-infrared source (Dey et al. 2005) shows unusually strong He II λ1640 lines *and* C IV lines in a localized region near the center of nebula, suggesting that this Lyα blob is powered, at least in part, by an obscured AGN. On the other hand, the absence of a C IV line in a spectrum with strong He II emission might indicate gravitational cooling gas like that in our simulations. As we discuss in the next section, the kinematics of the He II line can further constrain the origin of the He II emission. Second, if the AGN is heavily obscured, deep X-ray imaging of roughly megaseconds will provide the most direct probe, because X-rays from the AGN can penetrate the large column densities of gas and dust.

4.3. *Superwinds*

Alternatively, Taniguchi & Shioya (2000) suggest that galactic superwinds driven by starbursts could power the extended Lyα blobs. In this scenario, the collective kinetic energy of multiple supernovae is deposited into the surrounding gas, producing a superbubble filled with hot and high-pressure gas. If the mechanical energy overcomes the gravitational potential of the galaxies, this metal-enriched gas blows out into the surrounding primordial IGM and evolves into superwinds.

While the luminosity and sizes of the observed blobs are roughly consistent with the predictions of simple wind models, the mechanism to convert the mechanical energy into Lyα emission is not clear. Using a fast-shock model, Francis et al. (2001) show that if the shocks are radiative, the emission from the excited gas in the shock itself and the photoionized precursor region in front of the shock can explain the observed Lyα surface brightness of the blobs. For example, if we adopt the fiducial model of the prerun shock grids from L. Kewley et al. (2006, in preparation; MAPPINGS code by Dopita & Sutherland 1996) with a shock velocity of 700 km s^{-1}, a number density of 10^{-2} cm^{-3}, a magnetic parameter of $B/\sqrt{n} = 2\mu$G cm$^{3/2}$, and solar metallicity, then the Lyα and He II λ1640 emissivity from the shock+precursor region will be $\sim$0.04 and 0.002 ergs s^{-1} cm^{-2}, respectively. If the shock is perpendicular to our line of sight, we would expect surface brightnesses of $F_{\mathrm{Ly}\alpha} \sim 3 \times 10^{-18}$ and $F_{\mathrm{He\,II}} \sim 1.5 \times 10^{-19}$ ergs s^{-1} cm^{-2} arcsec^{-2} at $z = 3$. This Lyα surface brightness is roughly consistent with the observed mean surface brightness of Lyα blobs (Matsuda et al. 2004), but it is an underestimate if we consider that Lyα emission can be suppressed by various factors such as self-absorption and that the density of the IGM is possibly lower than the assumed density. If the IGM in the preshock region is composed of neutral primordial gas, the UV photons produced in the postshock plasma will ionize the preshock region, and the lack of an effective cooling mechanism other than the atomic hydrogen and helium lines can boost the Lyα and He II λ1640 line emissivities significantly. However, the low-metallicity shock grid is not currently available, and the density of the IGM in the preshock region and the effect of mixing between the metal-enriched winds and the pristine IGM are quite uncertain. Thus, it is difficult to predict how much mechanical energy is released through the Lyα or He II λ1640 lines in the superwind model.

One important feature of the superwind shock model is that it also predicts many UV diagnostic lines (e.g., C IV λ1549) that have been used to study the energetics of the narrow-line region in AGNs. The debate about the origin of the Lyα blobs arises mainly because Lyα is not a good diagnostic line to discriminate between AGN photoionization and superwind shock-excitation owing to its sensitivity to resonant scattering and obscuration by dust. Ideally, line ratios (e.g., He II/C IV), once detected, could be used to discriminate among the different mechanisms.

The kinematics of the blob is potentially another test of the superwind hypothesis, because of the expected bipolar outflow motion of the expanding shell. For example, Ohyama et al. (2003) claim that blob 1 of Steidel et al. (2000) shows both blueshifted and redshifted components ($\sim\pm$3000 km s^{-1}) in the central region, and they attribute these profiles to the expanding bipolar motion of a shocked shell driven by a superwind. On the other hand, using integral field spectrograph data, Bower et al. (2004) argue that blob 1 has chaotic velocity structures that can be explained by the interaction of slowly rising buoyant material with cooling gas in the cluster potential and that a powerful collimated outflow alone appears inconsistent with the lack of velocity shear across the blob.

We show in Figure 9 the He II λ1640 luminosity-weighted velocity dispersions of the gas particles associated with individual blobs. The effect of Hubble expansion and peculiar motion is included in the velocity dispersion calculations, but the thermal broadening for each gas particle is not. Most halos have velocity dispersions smaller than $\sim$400 km s^{-1}, compared to the typical superwind speed of several hundreds to a 1000 km s^{-1} (e.g., Heckman et al. 2000; Pettini et al. 2001). For the superwind case, because the observed Lyα emission comes mainly from the shock between the outflow from a galaxy and the surrounding pristine IGM, we expect the He II emission to be as extended as the observed Lyα emission. Therefore, if we observe a spatially resolved Lyα- *and* He II–emitting blob and its velocity dispersion is larger than 400 km s^{-1}, it is possible to exclude cooling radiation as the source of that blob. Note that there would be no ambiguities in measuring the size and line broadening, because He II λ1640 is optically thin. Thus, He II λ1640 is a finer tool than H I λ1216 to study the kinematic properties of Lyα blobs.

5. CONCLUSIONS

In this paper, we use high-resolution cosmological simulations to study the gravitational cooling lines arising from gas accreted by forming galaxies. Because baryons must radiate thermal energy to join a galaxy and form stars, accreting gas produces extended H I λ1216 emission (a "Lyα blob") surrounding the galaxy. We also expect cooling lines from singly ionized helium such as He II λ1640 to be present within Lyα blobs. We investigate whether three major atomic cooling lines, H I λ1216, He II λ1640, and He II λ304 are observable in the FUV and optical. We discuss the best observational strategies to search for cooling sources and how to distinguish them from other possible mechanisms for producing Lyα blobs. Our principal findings are as follows:

1. H I λ1216 and He II λ1640 (He II Baα) cooling emission at $z = 2$–3 are potentially detectable with deep narrowband imaging and/or spectroscopy from the ground. He II λ304 will

be unreachable until a large-aperture UV space telescope (e.g., *SUVO*; Shull et al. 1999) is available.

2. While our predictions for the strength of the H I λ1216 emission line depend strongly on how to handle the self-shielded gas, our predictions for the He II λ1640 line are rather robust owing to the negligible emissivity of He II for the self-shielded IGM below $T \sim 10^{4.5}$ K.

3. Although He II λ1640 cooling emission is fainter than Lyα by at least a factor of 10 and, unlike Lyα blobs, might not be resolved spatially with current observational facilities, it is more suitable to study gas accretion in the galaxy formation process because it is optically thin, less sensitive to the UV background, and less contaminated by recombination lines from star-forming galaxies.

4. To use the H I λ1216 and He II λ1640 cooling lines to constrain galaxy formation models, we first need to exclude the other possible mechanisms for producing Lyα blobs. First, because He II λ1640 emission from stars is limited to stars with very low metallicities [$\log(Z/Z_{\odot}) \lesssim -5.3$] and Population III objects, stellar populations, unlike the case of Lyα, cannot be responsible for its detection. Second, the kinematics of the He II λ1640 line can distinguish gravitational cooling radiation from a scenario in which starburst-driven superwinds power Lyα blobs, because the He II line width from cooling gas is narrower ($\sigma < 400$ km s^{-1}) than the typical wind speeds (which are factors of several higher). Third, if some fraction of the He II–emitting blobs are powered by AGNs, additional diagnostics, such as the C IV line and/or X-ray emission, can be used to discriminate gravitationally cooling blobs from those powered, at least in part, by AGNs.

We thank an anonymous referee for his/her thorough reading of the manuscript and helpful comments. We thank Mark Fardal, Dusan Keres, and Jane Rigby for valuable discussions. Y. Y. and A. I. Z. acknowledge funding from *HST* grant GO-09781.03-A, NASA LTSA grant NAG5-11108, and NSF grant AST 02-06084. N. K. and D. H. W. were supported by NASA NAGS-13308 and NASA NNG04GK68G. In addition N. K. was supported by NSF AST 02-05969.

REFERENCES

Aggarwal, K. M., Callaway, J., Kingston, A. E., & Unnikrishnan, K. 1992, ApJS, 80, 473
Barger, A. J., et al. 2003, AJ, 126, 632
Barton, E. J., Davé, R., Smith, J. T., Papovich, C., Hernquist, L., & Springel, V. 2004, ApJ, 604, L1
Binney, J. 1977, ApJ, 215, 483
Birnboim, Y., & Dekel, A. 2003, MNRAS, 345, 349
Bower, R. G., et al. 2004, MNRAS, 351, 63
Bromm, V., Kudritzki, R. P., & Loeb, A. 2001, ApJ, 552, 464
Cantalupo, S., Porciani, C., Lilly, S. J., & Miniati, F. 2005, ApJ, 628, 61
Cowie, L. L., Barger, A. J., Bautz, M. W., Brandt, W. N., & Garmire, G. P. 2003, ApJ, 584, L57
Davé, R., Dubinski, J., & Hernquist, L. 1997, NewA, 2, 277
Dekel, A., & Birnboim, Y. 2004, MNRAS, submitted (astro-ph/0412300)
Dey, A., et al. 2005, ApJ, 629, 654
Dopita, M. A., & Sutherland, R. S. 1996, ApJS, 102, 161
Fardal, M. A., Katz, N., Gardner, J. P., Hernquist, L., Weinberg, D. H., & Davé, R. 2001, ApJ, 562, 605
Francis, P. J., et al. 2001, ApJ, 554, 1001
Furlanetto, S. R., Schaye, J., Springel, V., & Hernquist, L. 2003, ApJ, 599, L1
———. 2005, ApJ, 622, 7
Haardt, F., & Madau, P. 1996, ApJ, 461, 20
Haiman, Z., & Rees, M. J. 2001, ApJ, 556, 87
Haiman, Z., Spaans, M., & Quataert, E. 2000, ApJ, 537, L5
Heckman, T. M., Lehnert, M. D., Strickland, D. K., & Armus, L. 2000, ApJS, 129, 493
Jakobsen, P. 1998, A&A, 335, 876
Katz, N., Keres, D., Dave, R., & Weinberg, D. H. 2003, The IGM/Galaxy Connection: The Distribution of Baryons at $z = 0$, ed. J. L. Rosenberg & M. E. Putman (Dordrecht: Kluwer), 185
Katz, N., Weinberg, D. H., & Hernquist, L. 1996, ApJS, 105, 19
Keel, W. C., Cohen, S. H., Windhorst, R. A., & Waddington, I. 1999, AJ, 118, 2547
Keres, D., Katz, N., Weinberg, D. H., & Dave, R. 2005, MNRAS, 363, 2
Leitherer, C., et al. 1999, ApJS, 123, 3
Malhotra, S., & Rhoads, J. E. 2004, ApJ, 617, L5
Martin, C. L., & Sawicki, M. 2004, ApJ, 603, 414
Matsuda, Y., et al. 2004, AJ, 128, 569
Møller, P., & Jakobsen, P. 1990, A&A, 228, 299
Murali, C., Katz, N., Hernquist, L., Weinberg, D. H., & Davé, R. 2002, ApJ, 571, 1
Oh, S. P., Haiman, Z., & Rees, M. J. 2001, ApJ, 553, 73
Ohyama, Y., et al. 2003, ApJ, 591, L9
Pettini, M., Shapley, A. E., Steidel, C. C., Cuby, J., Dickinson, M., Moorwood, A. F. M., Adelberger, K. L., & Giavalisco, M. 2001, ApJ, 554, 981
Schaerer, D. 2003, A&A, 397, 527
Schaerer, D., & Vacca, W. D. 1998, ApJ, 497, 618
Schaye, J., Aguirre, A., Kim, T., Theuns, T., Rauch, M., & Sargent, W. L. W. 2003, ApJ, 596, 768
Shapley, A. E., Steidel, C. C., Pettini, M., & Adelberger, K. L. 2003, ApJ, 588, 65
Shull, M., et al. 1999, The Emergence of the Modern Universe: Tracing the Cosmic Web (Boulder: UVOWG), http://origins.colorado.edu/uvconf/UVOWG.html
Steidel, C. C., Adelberger, K. L., Shapley, A. E., Pettini, M., Dickinson, M., & Giavalisco, M. 2000, ApJ, 532, 170
Storey, P. J., & Hummer, D. G. 1995, MNRAS, 272, 41
Taniguchi, Y., & Shioya, Y. 2000, ApJ, 532, L13
Telfer, R. C., Zheng, W., Kriss, G. A., & Davidsen, A. F. 2002, ApJ, 565, 773
Tran, K. H., Lilly, S. J., Crampton, D., & Brodwin, M. 2004, ApJ, 612, L89
Tumlinson, J., Giroux, M. L., & Shull, J. M. 2001, ApJ, 550, L1
Tumlinson, J., Shull, J. M., & Venkatesan, A. 2003, ApJ, 584, 608
Zheng, Z., & Miralda-Escudé, J. 2002, ApJ, 578, 33